BOLETIN DE LA SOCIEDAD ESPAÑOLA DE
Cerámica y Vidrio
www.elsevier.es/bsecv

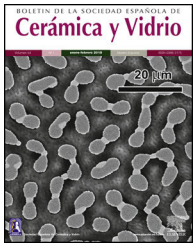

Praseodymium and gadolinium doped ceria as oxygen electrode for solid oxide cell applications

Miguel Ángel Morales-Zapata, Ángel Larrea, Miguel Ángel Laguna-Bercero*

Instituto de Nanociencia y Materiales de Aragón, CSIC-U, Zaragoza, c/ María de Luna 3, 50018 Zaragoza, Spain

ARTICLE INFO

Article history:
Received 3 September 2024
Accepted 13 March 2025
Available online 10 April 2025

Keywords:
Solid oxide fuel cells
Doped ceria
Air electrode

ABSTRACT

This study analyzes the structural and electrochemical properties of praseodymium- and gadolinium-doped ceria (CPGO) samples formed by the sintering reaction of $Pr_2NiO_{4+\delta}$ (PNO) and $Ce_{0.9}Gd_{0.1}O_{2-\delta}$ (GDC). X-ray powder diffraction analysis confirmed a single-phase cubic CPGO structure as a primary phase. The cationic compositions were determined using energy dispersive spectroscopy (EDS) in a scanning transmission electron microscope (STEM), while core-loss electron energy-loss spectroscopy (EELS) was used to determine the valence of Ce and Pr. The compatibility between thermal expansion coefficients validated their integration with electrolytes at the typical Solid Oxide Cell (SOC) operation temperatures. Oxygen chemical diffusion and surface exchange coefficients were investigated using the electrical conductivity relaxation (ECR) method at intervals of partial oxygen pressures between 0.10 and 0.21 atm and 600 °C and 800 °C. Finally, the samples were tested in symmetrical cells by electrochemical impedance spectroscopy (EIS) between 700 °C and 850 °C. A polarization resistance of 0.17 Ω cm^2 at 850 °C was obtained for CPGO air electrodes formed by sintering a mixture of 80% by weight of GDC and 20% by weight of PNO. These findings confirm that PNO–GDC mixtures forming CPGO oxides are excellent candidates for SOC applications.

Ceria dopada con praseodimio y gadolinio como electrodo de oxígeno para aplicaciones en pilas de óxido sólido

Palabras clave:
Pilas de combustible de óxido sólido
Ceria dopada
Electrodo de aire

RESUMEN

En este estudio se analizan las propiedades estructurales y electroquímicas de composites formados por la reacción de sinterización de $Pr_2NiO_{4+\delta}$ (PNO) y $Ce_{0.9}Gd_{0.1}O_{2-\delta}$ (GDC). Los refinamientos de Rietveld de los patrones de difracción de rayos X confirmaron una estructura cúbica monofásica de ceria dopada con praseodimio y gadolinio (CPGO) como fase primaria.

* *Corresponding author.*
E-mail address: malaguna@unizar.es (M.Á. Morales-Zapata).
https://doi.org/10.1016/j.bsecv.2025.03.003

Las composiciones catiónicas de CPGO se determinaron mediante espectroscopia de dispersión de energía (EDS) en un microscopio electrónico de transmisión de barrido (STEM), mientras que se utilizó espectroscopia de pérdida de energía de electrones (EELS) para determinar la valencia de Ce y Pr. La compatibilidad entre coeficientes de expansión térmica validó la integración de los electrodos con electrolitos a las temperaturas de operación típicas de las pilas de óxido sólido (SOC). Los coeficientes de difusión química de oxígeno y de intercambio superficial se determinaron mediante relajación de la conductividad eléctrica (ECR). Finalmente, se caracterizaron celdas simétricas mediante espectroscopia de impedancia electroquímica (EIS), obteniendo una baja resistencia de polarización de 0.17 $\Omega\,cm^2$ a 850 °C para electrodos de aire compuestos por 80% de GDC y 20% de PNO en peso. Estos hallazgos confirman que los electrodos de CPGO son excelentes candidatos para aplicaciones SOC.

Introduction

Ruddlesden–Popper (RP) lanthanide nickelate materials are of current interest for their potential application as air/oxygen electrodes in solid oxide fuel cells (SOFC) and solid oxide electrolysis cells (SOEC), oxygen pumps, oxygen sensors and catalytically active membranes for membrane reactors, as they present mixed electronic and ionic conductivities [1]. These innumerable applications are possible due to their high surface exchange (k_{ex}) and chemical diffusion (D_{chem}) coefficients being comparable with that of other solid oxide cells (SOC) materials, like perovskites and double perovskites [2,3]. Among the lanthanide nickelates, $Pr_2NiO_{4+\delta}$ (PNO) demonstrates the highest rate of surface exchange activity in comparison with manganite or cobaltite-based materials [4], also displaying the highest oxygen diffusivity among the nickelates in literature [5].

The most prominent issue with nickelate-based electrodes is their reactivity with standard electrolyte materials, which induces the formation of insulating phases that increase the polarization resistance (R_{pol}) [6]. Even so, several studies have demonstrated that nickelates are among the most promising oxygen electrodes for electrolysis applications [7,8]. With the particular use of ceria-based electrolytes, high-resistivity phases are not formed, and the cell performance can achieve stability over time [9]. The air electrode/electrolyte compatibility has been studied for gadolinium-doped ceria (GDC), yttria-stabilized zirconia (YSZ), and lanthanum–strontium–gallium manganite (LSGM), revealing that YSZ and GDC are highly reactive with PNO at 900 °C for over 24 h, while reactivity is not as evident in LSGM for up to 72 h at 1000 °C [10]. In the presence of GDC, PNO decomposition into PrO_x and $Pr_4Ni_3O_{10-\delta}$ without further formation of NiO occurs at 800 °C [11], as well as the formation of cubic fluorite Pr- and Gd-doped ceria phases (CPGO) [12]. These composites were electrochemically tested on oxygen electrodes fabricated from PNO and GDC mixtures on single-microtubular cell configurations [12]. This configuration was also characterized for 150 h of combined reversible SOFC/SOEC operation without degradation of the air electrode [13]. Similarly, ceria and PNO mixtures have been used as diffusive layers to repel the formation of insulating phases in planar cells [14]. Even with interdiffusion, the degradation rate of the PNO–GDC system is low in the long term [15], while featuring more suitability than YSZ and SSZ at intermediate temperatures [16] due to the lower densification of the ceria that can prevent the agglomeration of particles. It has also been demonstrated that CPGO interlayers diminish the nickelate decomposition and boost the SOFC power density [17].

The CPGO phase formed by the PNO–GDC interaction is analogous to the $Ce_{1-x}Pr_xO_{2-\delta}$ (PDC) lanthanide-ceria system, known for its high oxygen availability [18,19] and high electrical conductivity [20,21]. Increasing the praseodymium content in PDC also increases the oxygen vacancy concentration and the total conductivity of the material [22]. This effect benefits SOC air electrodes, where a mixed oxide with a composition near $x = 1$ (single-phase) is the most favorable composition for an active layer. However, many authors have reported a high thermal and chemical expansion for these oxides [14,23], although, for $x < 0.2$, the thermal and chemical expansions seem to be more suitable for SOFC operation [24].

This article reflects on the structural and electrochemical characterization of CPGO compositions formed by sintering reactions of PNO and GDC. These mixtures have demonstrated good compatibility with YSZ electrolytes, confirming their interest as air electrodes for SOCs [12]. However, previous studies do not delve into the structural, kinetic, and electrochemical of these oxides in air electrode applications for SOC. This study intends to compare the behavior of these properties between doped ceria and PNO electrodes. For this purpose, we have selected different PNO and GDC mixed oxide compositions obtained by sintering at 1450 °C. The ratio compositions were chosen to verify the limits of interdiffusion of praseodymium into the ceria lattice and the possible influence of the secondary phases on the electrochemical performance of PNO–GDC electrodes. The basis for selecting the same sintering temperature for composites with different PNO content is to ensure the high density of the samples, particularly in ceria. The structural studies of the air electrodes include X-ray diffraction (XRD) and dilatometry experiments, focusing on the effect of cation interdiffusion at high-temperature sintering and thermal expansion at usual SOC operation temperatures. Energy dispersive spectroscopy (EDS) and electron

energy-loss spectroscopy (EELS) are performed to determine the elemental composition of the CPGO phases and to track possible Ce and Pr valence changes. We also focus on the electrochemical performance via the electrical conductivity relaxation method (ECR), measuring the k_{ex} and D_{chem} coefficients, as the time domain analysis of the ECR response is based on the "ideal" behavior of the diffusion process. This approach is applied to the system, previously obtaining the changes in the driving force from a resulting oxygen flux [25]. Finally, electrochemical impedance spectroscopy (EIS) analyses are conducted in symmetrical cells to validate their SOC electrode performance.

Experimental

Sample preparation

The samples are prepared from commercial ceramic powders $Pr_2NiO_{4+\delta}$ (Marion Technologies) and $Ce_{0.90}Gd_{0.10}O_{1.95}$ (GDC10-M, Fuelcell Materials), mixed with polyvinyl alcohol in an agate mortar at a ratio of 0.15 ml per gram of the powder mixture, until a uniform compound was visible and then inserted into a latex sheath to form cylindric samples. The bars are then uniaxially pressed at 2000 bar and sintered at 1450 °C for 2 h at a rate of 5 °C min^{-1}. The samples were structurally and microstructurally evaluated in three different PNO–GDC compositions: 20% GDC + 80% PNO by weight (C20), 80% GDC + 20% by weight (C80), and 100% PNO for comparison. The approximate dimensions of the samples were about 7.0 × 2.5 (length × diameter in mm^2). For the electrochemical studies, symmetrical cells were also prepared using >98% dense GDC pellets as electrolytes, with a diameter of ∼18 mm and thickness of ∼1.2 mm. In this configuration, thick and dense GDC electrolytes ensure that no electronic leakage is taking place at high temperatures. Electrode slurries (terpineol-based) of PNO and C80 compositions were fabricated and then deposited on both sides of GDC pellets, and subsequently sintered at 1100 °C for 2 h in air.

X-ray diffraction and dilatometry tests

XRD patterns of the milled powders were collected using Cu-Kα radiation in a D-Max Rigaku instrument. XRD powder analysis was performed using the FullProf Suite [26] for phase quantification and lattice parameter determination. Dilatometry tests under air were performed on the prepared air electrodes at a rate of 2 °C min^{-1} from RT to 1450 °C using a thermomechanical dilatometer analyzer (Setaram, SETSYS 200).

The XRD analysis is performed with crystal structure files retrieved in the CIF format from the Inorganic Crystal Structure Database (ICSD) database from FIZ Karlsruhe [27]. The structure information is converted to PCR format to process the XRD datasets with the LeBail and Rietveld methods using the Fullprof software [26]. With the LeBail method, the main crystalline phases and lattice parameters are identified by the search-match process of extracting the 2θ positions of the measured peaks and comparing them to the peak positions of all known phase structural models stored in a database. This procedure is followed by a Rietveld refinement to obtain the phase quantification of, where phases with peak positions matching the observed ones are added to the refinement project. The final Rietveld refinement parameters are provided in the Supplementary Information (ESI) document in Section S.2.

EDS-STEM and EELS

For the quantitative compositional analysis of the samples, energy dispersive spectroscopy in a scanning transmission electron microscope (EDS-STEM) was performed with an Ultim Max detector (Oxford Instruments) installed in an aberration-probe-corrected STEM (Titan from Thermo Fisher Scientific) operated at 300 kV. Energy dispersive spectra were collected in 0.20 eV/channel bins. The Cliff–Lorimer method for thin specimens [28] was applied using experimental profiles to ensure maximum fitting accuracy. INCA software from Oxford Instruments was employed for fitting, as the newest Oxford Instruments Aztec software does not include the option of defining our experimental profiles. The Cliff–Lorimer K_{GdCe}, K_{PrCe} and K_{NiPr} sensitivity factors were obtained from GDC, PDC, and PNO powder reference samples (Fig. S.1 in ESI). The cation ratio of these samples was determined by the Inductive Coupled Plasma (ICP) technique. The experimental peak profiles were obtained from Ce, Pr, Gd, and Ni oxides. In this analysis, the selected experimental profile peaks for fitting were Ce-L, Pr-L, Gd-L, and Cu-K. These peaks were used to improve the quantification accuracy because of the overlapping of Gd-Lα^1 (6.058 keV) and Ce-Lγ^1 (6.052 keV) lines, and the low levels of Gd and Pr atomic content in C20 and C80, respectively (the fitted spectra is shown in Fig. S.1 of the ESI). Thin TEM specimens were prepared by depositing acetone powder suspensions onto holey carbon Cu grids, except for NiO and Gd_2O_3 profile samples, in which Au grids were employed as Ni-K and Gd-L are too close to the Cu-K lines. Time acquisition was selected to obtain a quantification error (produced by the statistical counting fluctuations) lower than 1%. The experimental errors were estimated using a two-sigma criterion (95% confidence level).

Electron energy-loss spectra (EELS) were acquired in the same STEM as EDS using a Tridiem spectrometer (Gatan) to determine the variations of the oxidation state of Ce and Pr in the CPGO phase. For this purpose, Ce and Pr core-loss spectrum ranges were recorded for the same particles (CPGO and PNO) where the EDS-STEM analysis was performed. The collection semi-angle employed was 51.3 mrad with a convergence semi-angle of 24.8 mrad. The data were acquired with an energy dispersion of 0.20 eV per channel. The spectra obtained were analyzed using the Gatan® Digital Micrograph (DM) software. The core-loss peak intensity error is calculated according to Egerton [29], where the background is sampled only on the low-energy side of the ionization edges and is extrapolated to higher energies.

Electrical characterization

Electrical conductivity relaxation (ECR) measurements were performed by the four-probe technique using a Zahner Zennium galvanostat/potentiostat by obtaining voltage values

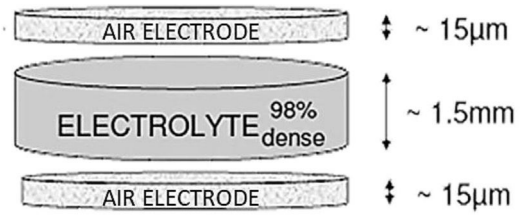

Cell	Air electrode	Configuration
PNO_CELL	PNO single layer	PNO/GDC/PNO
C80_CELL	C80 single layer	C80/GDC/C80
PNO-C80_CELL	C80 inner layer and PNO outer layer (7.5 µm each)	C80+PNO/GDC/C80+PNO

Fig. 1 – Schematic description of the symmetrical cells fabricated for electrochemical characterizations.

Table 1 – Samples used in this study. The phase ratios and lattice parameters were obtained from the XRD analysis, while the CPGO elemental compositions were determined by EDS-STEM.

Sample	Nominal composition (% by weight)	Density after sintering	Phases identified (% by weight)	Lattice parameters (Å)
PNO	PNO	>99%	95% PNO (primary phase)	5.3966(6); 5.4474(8); 12.4332(12)
			2% NiO	–
			3% $Pr_4Si_3O_{12}$	–
C20	20% GDC 80% PNO	>98%	38% $Ce_{0.301\pm0.006}Pr_{0.672\pm0.006}Gd_{0.028\pm0.006}O_{2-\delta}$	5.4013(5)
			27% PrO_x	5.4577(7)
			9% PNO	5.3913(9); 5.4439(5); 12.4395(7)
			25% NiO	–
C80	80% GDC 20% PNO	>95%	97% $Ce_{0.747\pm0.004}Pr_{0.162\pm0.004}Gd_{0.092\pm0.004}O_{2-\delta}$ (primary phase)	5.4134(3)
			3% NiO	–

over time with a current fixed at 10 mA. The temperature was measured with a thermocouple near the sample (within 2 mm). The cylindrical samples were placed into a Probostat test cell (NorECs) and inserted vertically into a tubular furnace. The temperature dependence of the oxygen transport properties was measured by changing the temperature stepwise from 800 to 600 °C. All the experiments were performed by changing pO_2 ranges from 0.21 to 0.10 atm. The total flux stream was fixed at 83 ml min^{-1}. ECR parameter fitting in this study was analyzed using the MATLAB toolbox ECRTOOLS [30], under a modified cylindrical geometry model.

Symmetrical cells were characterized by EIS to verify the electrochemical performance of the electrodes in air. The air electrode layers were sintered (at 1100 °C for 2.0 h) on GDC pellets with up/down ramps of 2 °C min^{-1}. The measurements were performed without current load using 20 mV of AC sinusoidal amplitude and a frequency range from 100 kHz to 100 mHz using a Zahner Zennium electrochemical station. The symmetrical cell configurations are described by the scheme of Fig. 1. In this study, we employ three different air electrode configurations: PNO_CELL (using only PNO as electrodes), C80_CELL (using C80 as air electrodes), and PNO–C80_CELL (a double-layered electrode with a configuration PNO/C80/GDC/C80/PNO), as described in Fig. 1. The electrical contacts are constructed using annealed gold wires of 0.25 mm in diameter and covered with gold paint to improve the electrical contact with the sample surface.

Results and discussion

Compositional, structural, and microstructural analysis

Sample composition

The phase composition of the samples is presented in Table 1. The PNO sample contained about 5% by weight of secondary phases: NiO and $Pr_4Si_3O_{12}$. This silicate phase, likely formed during the processing of the raw powder from the supplier, has also been observed in the analog neodymium nickelate (NNO [31]). NiO is likely produced from the nickelate decomposition over 700 °C and its effect on the electrical conductivity is almost negligible because of the low content.

The C20 sample presented mainly two fluorite phases corresponding to CPGO and PrO_x. The coexistence of these phases

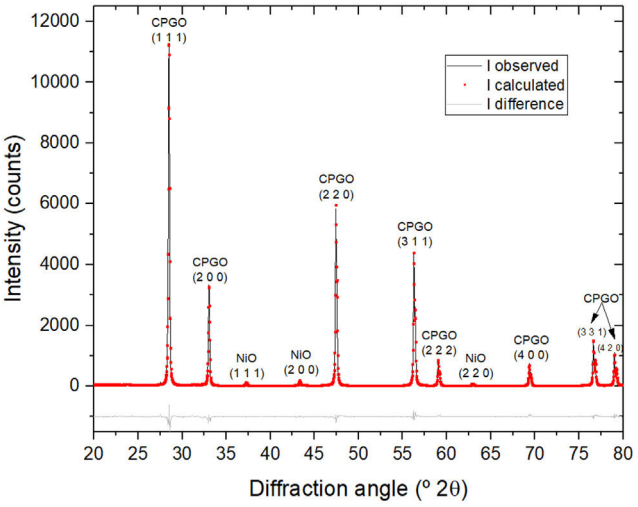

Fig. 2 – Experimental and calculated X-ray powder diffractogram of the C80 sample.

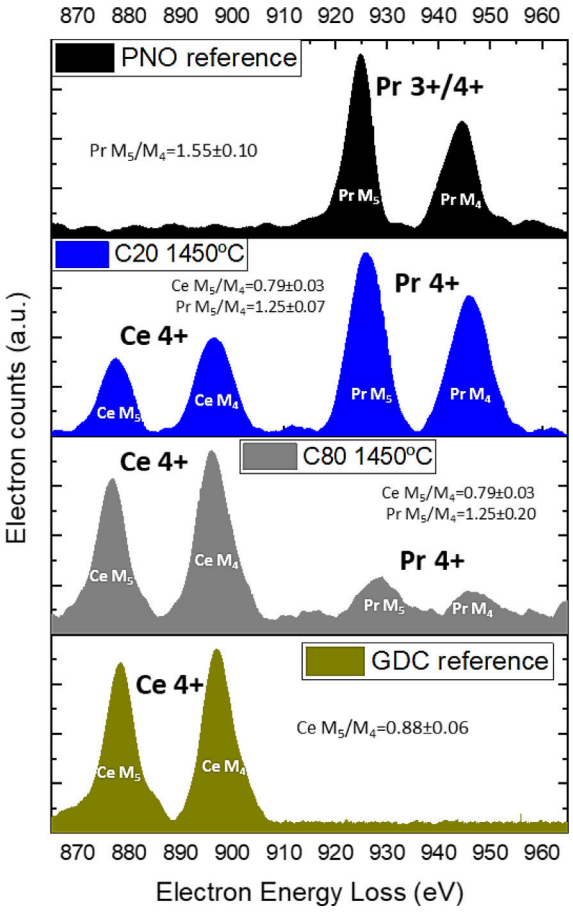

Fig. 3 – Background-subtracted EELS of M4 and M5 edges for CPGO particles in C20 and C80, compared with PNO and GDC reference samples.

has been previously reported [20,32]. The interest in the PNO-rich ceria composition is derived from the previously reported good performance in single SOC as a barrier layer for PNO air electrodes [12]. In addition to the fluorite phases, unreacted PNO and NiO are also present in C20. Fig. S.3 of the ESI shows isolated PNO particles of around 100 μm by diameter, which probably accounts for the high non-homogeneity of the sample as the nickelate is not fully decomposed. On the other hand, the C80 phase is composed almost entirely of a single fluorite phase (around 97% by weight). The presence of this phase indicates that a chemical diffusion of Pr into the ceria lattice is taking place [12,19]. Also, there is no unreacted PNO phase in the C80 sample. The NiO phase found in this sample is about 3 wt% and we did not observe any reactivity of the ceria by any of the methods described in this work. The reported limit of solubility of NiO in the ceria is about 10 to 12 mol% according to Barrio et al. [33]. As the Ni content in the sample is low, we could assume that the remaining Ni was dissolved into the fluorite ceria structure.

Other studies with higher NiO content mixed with the ceria (50 mol%) only reported a yield of 3 mol% of total Ni-content dissolved in the tetragonal solid solution in our case, according to the Rietveld refinement results [34].

According to McCullough [32], the secondary phases in Ce–Pr–O systems tend to disappear as the Pr content diminishes under 65% by weight. Also, under operating conditions, the coexistence of CPGO and GDC has been previously outlined [11].

The X-ray powder diffractogram of C80 is shown in Fig. 2. The parameters obtained from the Rietveld refinement are given in Table S.2 of the ESI. The weight composition obtained was 97.14% CPGO and 2.86% NiO, with no evidence for the presence of the PrO_x phase, according to the best fit ($\chi^2 = 1.87$).

Elemental composition of the CPGO phase

Cation interdiffusion into the ceria lattice is determined by quantification of the CPGO phase by EDS-STEM, as reported in Table 1. For the quantifications, particles of the CPGO phase contained in the C80 sample (18 grains of 150 nm of diameter on average) and C20 (15 grains of 135 nm of diameter on average) were analyzed. Selected particle microstructures and X-ray spectra are shown in Fig. S.2 of the ESI. The C20 Pr content (67% by atom) approaches the reported limits of solubility of Pr into ceria at around 70% by atom similar to PDC [20]. On the contrary, the Ce-Pr ratio of the CPGO phase in C80 was 4.6 with about 9% of Gd by atom.

Ce and Pr oxidation states

The oxidation states of Ce and Pr in CPGO were identified by EELS-STEM analysis of single-phase grains. We employed this analysis on four particles of 100 nm of diameter on average, in both C80 and C20, comparing the intensity ratios of the characteristic M_4 and M_5 EELS edges of Ce and Pr after background subtraction using a power-law model. These lines represent the $3d_{3/2} \rightarrow 4f_{5/2}(M_4)$ and $3d_{5/2} \rightarrow 4f_{7/2}(M_5)$ electronic transitions [35] and the peak intensity ratio points out the oxidation state [36]. Briefly, a significant presence of the 3^+ valence state is reflected in the increase of the intensity of the M_5 peak (and consequently in the M_5/M_4 ratio) with respect to 4^+ valence state.

The M_5/M_4 peak intensity ratio from GDC (Ce^{4+}) and PNO (mostly Pr^{3+}) reference samples are compared with the values

obtained for CPGO in C20 and C80 in Fig. 3. The obtained Ce M_5/M_4 peak intensity ratio reference for Ce^{4+} was 0.88 ± 0.06, in good agreement with previous experiments [37], while for CPGO it was 0.79 ± 0.03 in both PNO–GDC air electrodes. The Ce $M_{4,5}$ peaks in C20, C80, and GDC have the same intensity relationship showing a tendency for the Ce^{4+} oxidation state. Other authors also found Ce^{4+} in PDC solid solutions under oxidation conditions using EELS [38] and X-ray absorption near-edge spectra (XANES) [39] experiments. The calculated Pr M_5/M_4 ratio is 1.25 ± 0.07 for C20 and 1.25 ± 0.20 for C80. Although the relative error in C80 is high, both values are compatible with the one obtained for Pr^{4+} ($M_5/M_4 \sim 1.28$) [35]. These results confirm the expected Pr^{4+} valence for Pr-doped ceria, as reported in many works [20,32]. This is a good indicator of a possible formation of a high entropy oxide as it favors the incorporation of the dopant into the host lattice, a product of a similar cation size in the dopant and host cation at the same oxidation state. Similarly, EELS M_5/M_4 ratio analyses consistently match the results obtained for the CPGO lattice parameter predictions with the presence of Ce^{4+} and Pr^{4+}. Schaube et al. [40] highlighted the importance of point defects for oxygen surface reaction kinetics on doped ceria by PIE experiments. They mentioned that at a higher temperature, the Pr^{3+} incorporated into the ceria tends to approximate the total Pr content; however, at increasing pO_2, the Pr^{3+} content diminishes. Other authors mentioned that the Pr oxidation state at the surface of PDC deviated significantly from that of the bulk [41,42] Fig. 4.

In PNO reference samples, the Pr M_5/M_4 peak intensity values obtained for as-received and sintered PNO were 1.55 ± 0.10 and 1.52 ± 0.07, respectively. These values indicate a mixed $3^+/4^+$ valence for Pr according to the expected values in the literature for the Pr M_5/M_4 ratio [43,44].

As sample C20 presents a high degree of inhomogeneity, it has been discarded from further structural and electrochemical studies. This phase is presented in this section only to determine the solubility limits of PNO in the doped ceria and its structural and microstructural properties in comparison to PNO and C80. The interest in a more stable CPGO phase formation led this analysis toward a focus on the C80 sample, for all the subsequent characterizations.

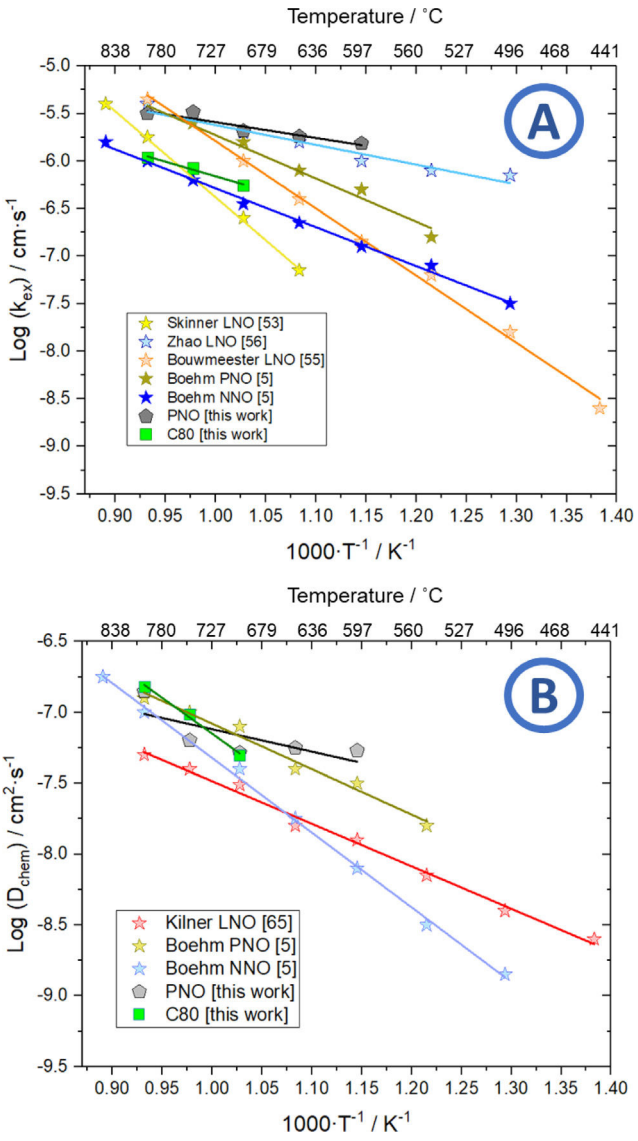

Fig. 4 – Temperature dependences of k_{ex} (a) and D_{chem} (b) for the samples studied in this work compared with nickelate literature data.

Lattice parameter

Table 1 presents the lattice parameters for samples PNO and C80. The lattice parameters of the nickelate phase reported are consistent with literature values [12]. C80 presents a similar pattern between the lattice parameter and the Pr content in CPGO, according to Kim's empirical method [45] and previous CPGO experiments [23]. The lattice parameters of CPGO follow a linear function of Vegard's rule as CPGO has a fluorite-type cubic crystal structure, and the ionic radii of Pr^{4+} and Ce^{4+} are similar. From our calculations, the average Pr oxidation state is 3.94 in C80 ($16.2 \pm 0.4\%$ Pr by atom), which is in good agreement with the EELS estimations. The obtained experimental value in C80 ($a = 5.4134$Å for $16.2 \pm 0.6\%$ Pr by atom) is also compatible with the recorded by Cheng et al. [23] ($a = 5.4146$Å for 15% of Pr by atom). Cheng et al. [23] investigated the lattice parameters evolution with the composition of dopants (Pr, Gd), obtaining theoretical parameters in good agreement with the experimental ones. While Kim's method adjusts well with our experimental data for C80, the data from Cheng et al. does not follow this kind of linearity because the Gd content is a constant (10% by atom).

Thermal expansion coefficient

The thermal expansion coefficient (TEC) of C80 was measured from RT to 1450 °C (Fig. S.4a in ESI) using the method of differences [46] for a first-order phase transition (refer to ESI section S.2). In this temperature range, the mean TEC for C80 was $14.1 \times 10^{-6}\,K^{-1}$, slightly higher than for YSZ and GDC electrolytes $\sim 12 \times 10^{-6}\,K^{-1}$ [47]. However, the coefficients rose to about $18.1 \times 10^{-6}\,K^{-1}$ and $19.1 \times 10^{-6}\,K^{-1}$ for C80 at 700 °C (Fig. S.5 in ESI). Similar changes were noticed by several authors [14,22,48]. These reports suggest a phase transition and could explain the transition temperatures at 650 °C (Fig. S.4a). Chockalingam et al. [14] noted this transition of CPGO in $Ce_{0.75}Pr_{0.20}Gd_{0.05}O_{2-\delta}$, a similar composition to C80.

Table 2 – Activation energy values for oxygen surface exchange and diffusion processes in $Ln_2NiO_{4\pm\delta}$ (Ln = La, Pr, Nd) and $Ce_{0.9}Gd_{0.1}O_{2-\delta}$ mixed oxides at selected temperature ranges and pO_2 = 0.21 atm.

Oxide	ΔT, °C	Activation energy (eV)		Method	Reference
		Diffusion	Exchange		
LNO	450–800	0.62	1.29	SIMS	Kilner et al. [65]
	600–800	n/a	1.35	PIE	Bouwmeester et al. [56]
PNO	520–800	0.71	0.41	SIMS	Boehm et al. [5]
	550–700	1.05	1.46	PIE, ECR	Saher et al. [59]
	550–750	0.91	1.44	PIE, ECR	Sadykov et al. [58]
	700–800	0.88 ± 0.33	0.38 ± 0.25	ECR	This work
	600–800	0.40 ± 0.16	0.29 ± 0.06	ECR	This work
C80	700–800	1.00 ± 0.08	0.61 ± 0.06	ECR	This work
NNO	520–800	1.07	0.78	SIMS	Boehm et al. [5]

Chiba et al. [22] also observed the same transition at 450 °C for $Ce_{0.3}Pr_{0.7}O_{2-\delta}$ and at ~550 °C for $Ce_{0.8}Pr_{0.2}O_{2-\delta}$ This may be related to the ceria temperature of reduction at the surface (around 420 °C) and in bulk (around 720 °C) [49]. The intermediate state is caused by a thermodynamic factor (equilibrium concentration of oxygen vacancies driven by temperature and oxygen pressure) and a kinetic factor (oxygen diffusion rates in the crystal and ordering of vacancies). The increase in the slope of the curves at high temperatures may be due to the loss of lattice oxygen [14]. Doping praseodymium into ceria induces significant chemical expansion [14,50] that affects the thermomechanical stability of the material. Cheng et al. [23]. found an increase of TEC with the Pr concentration due to a chemical expansion, especially when trying to match the electronic conductivity in the range of ionic conductivity, where more than 12.5% of Pr by atom is needed.

Finally, the change of slope of TEC for C80 in the 650–700 °C range of Fig. S.5 is probably related to PNO decomposition, which starts at 700 °C [51], expelling PrO_x at 800 °C [52] that is later incorporated into the cubic ceria fluorite structure producing a lattice expansion and forming the new CPGO phase. This is exemplified by the contraction velocity calculations from dilatometry tests in both PNO–GDC samples, where a peak is observed at around 1100 °C (Fig. S.4b in ESI).

Determination of surface exchange and chemical diffusion coefficients

The k_{ex} and D_{chem} values for lanthanide nickelates at different temperatures are extracted from several sources [5,53–59] and shown as a comparison to the C80 and PNO electrodes in Fig. 4a and b. ECR fitting examples can be found in Fig. S.8. In general, the coefficients are in good agreement with lanthanide nickelates [5,54,60] and doped ceria [40,58,61,62]. The k_{ex} coefficient is directly associated with electrocatalytic activity and oxygen reduction reaction (ORR) rate. On the other hand, D_{chem} is not significantly influenced by the morphology of particles, being more affected by ionic conductivity. The most likely mechanism of diffusion is influenced by apical and interstitial oxygen.

Table 2 summarizes the apparent activation energies for k_{ex} and D_{chem}. The activation energy of PNO's coefficients agrees with the SIMS data [5] in the 700–800 °C range. As seen in Table 2, PNO's activation energies of k_{ex} (0.38 eV) and D_{chem} (0.88 eV) in the 700–800 °C range do not differ significantly from Boehm et al. [5] (0.41 and 0.71 eV, respectively). However, below 700 °C energy decreases which could be influenced by the ECR method. In ECR, the measurements can be in surface, diffusion, or mixed control regimes [30]. Fittings to relaxation data with a lower than 3% standard error mean a re-equilibration in a mixed regime in oxygen kinetic coefficients. The surface-controlled regime, where the estimation of D_{chem} has higher uncertainty, is usually found at low temperatures, while diffusion control can be seen at higher temperatures. This means that k_{ex} values have a higher error at temperatures higher than 650 °C as they enter the diffusion regime. A higher error in activation energies was observed in the oxygen surface for PNO-rich samples.

Ciucci et al. [30] highlighted the mass transport analogy of Biot number and sensitivity to investigate the measurability of the oxygen diffusion coefficients. In this model, the ECR method considers that the parameters governing the sensitivity are linked to the Biot number, the diffusion and reaction timescales. For a small Biot number, the ECR experiment is sensitive only to oxygen surface exchange, while for a large Biot number only the oxygen diffusion is identifiable. We calculated this relation for the values obtained (Fig. S.9 in the ESI), showing that most of the calculations for k_{ex} and D_{chem} are within the mixed oxygen chemical diffusion and surface exchange control regime. However, the PNO-rich samples approach the oxygen chemical diffusion control regime.

In C80, under similar conditions, the reported activation energy of GDC in the D_{chem} process is 1.1 eV, while for k_{ex} is 1.0 eV below 650 °C [63,64]. The same authors suggested a change in activation energies over 650 °C at 2.4 eV, which is higher than the 0.61 eV obtained in our calculations between 700 and 800 °C.

Electrochemical characterizations

Electrical conductivity

The electrical conductivity of C80 maintains values up to $\sigma = 0.13\ S\,cm^{-1}$ at 800 °C, while in PNO the electrical conductivity is $\sigma = 93.19\ S\,cm^{-1}$ at 800 °C, as shown in Figs. S.6 and S.7 of the ESI. Those values are consistently within the same range as those reported in the literature for PNO [5], PDC [22,66], and CPGO [14,22]. PNO conductivity is substantially higher than the ceria compounds due to the presence of conductive $PrNiO_3$ perovskite layers in the RP structure.

The C80 sample also presents a higher conductivity than GDC, likely driven by a Pr-impurity that narrows the gap between conduction and valence bands. In literature, diverse GDC electrical conductivity values are reported at 800 °C ranging from 5×10^{-4} to 2×10^{-2} S cm^{-1} [67,68], while for PDC, there seems to be an increase of electrical conductivity proportional to the Pr content [69]. For C80, it is important to consider that Pr doping facilitates electronic transition by the formation of an impurity band in between the O-2p valence band and the Ce-4f conduction band [70,71]. Minor dopant additions do not influence ceria-based compounds' total and ionic conductivity. The contribution of the electron/hole conductivity to the total conductivity increases with temperature, with a significantly lower activation energy for ionic conduction (0.7–0.8 eV) than for p-type electronic transport (1.1–1.7 eV) [70]. The activation energy calculated for electronic conductivity in C80 was 1.40 eV. As a comparison, the activation energy for electronic conductivity of low Pr content CPGO phases is 1.10 eV [67].

EIS measurements on symmetrical cells

Finally, EIS measurements of the PNO cell and the C80 cell (refer to Fig. 1 for the cell configurations) were carried out and the results are compared in Fig. 5a. Similarly, these cells are compared with the PNO-C80 cell to evaluate the performance of C80 as a barrier active layer. The symmetrical cells were evaluated by a distribution of relaxation times (DRT) to assess the changes of either PNO or the doped ceria composition on the electrode microstructure, and the mechanisms that contribute to the deconvoluted peaks of the R_{pol} in Fig. S.10 and Table S.3. At 850 °C, the R_{pol} value of PNO cell (0.53 Ω cm^2) is three times higher than in C80 cell (0.17 Ω cm^2).

According to the existing literature [72] for similar electrodes, the processes from the DRT data could be identified as follows: electron transfer between the electrode and current collector (P1), oxygen ion transfer across the electrodes and the electrolyte interface (P2), oxygen surface exchange (P3), and oxygen diffusion (P4).

DRT peak deconvolution results shown in Fig. 5c, describe how the composition or temperature affects the P1 peak in the 10^4 and 10^5 Hz frequency range. Such a high-frequency mechanism is typically associated with interfacial effects in the electrode [73]. The performance of peaks P1 and P2 is similar for C80_CELL and PNO-C80_CELL, however, the compensation effect of the reduction of peaks at lower frequencies suggests an important increase of the effective electrochemically active sites at the electrode/electrolyte interface at 800 °C when using the single C80 layer. In the C80 cell at 850 °C, P1 is higher, and this process is thermally driven in the order of PNO-C80 > C80, possibly influenced by the ceria phase reduction. P2 peaks were generally lower in PNO and PNO-C80 cells, suggesting higher activation than in C80 cell. Also, the double-layered symmetrical cells (PNO-C80) presented a similar behavior with a slight R_{pol} increase over single-layer cells, indicating that the PNO current collector layer does not affect the performance significantly. However, some effects are observed in Fig. 5c, where DRT peaks between 10^2 and 10^5 Hz show an improvement of the PNO air electrode when including a barrier layer of C80 in the electrolyte interface. When it comes to the single air electrode layer in C80_CELL, the peaks are considerably diminished below the 10^4 Hz range. In the C80 and PNO-C80

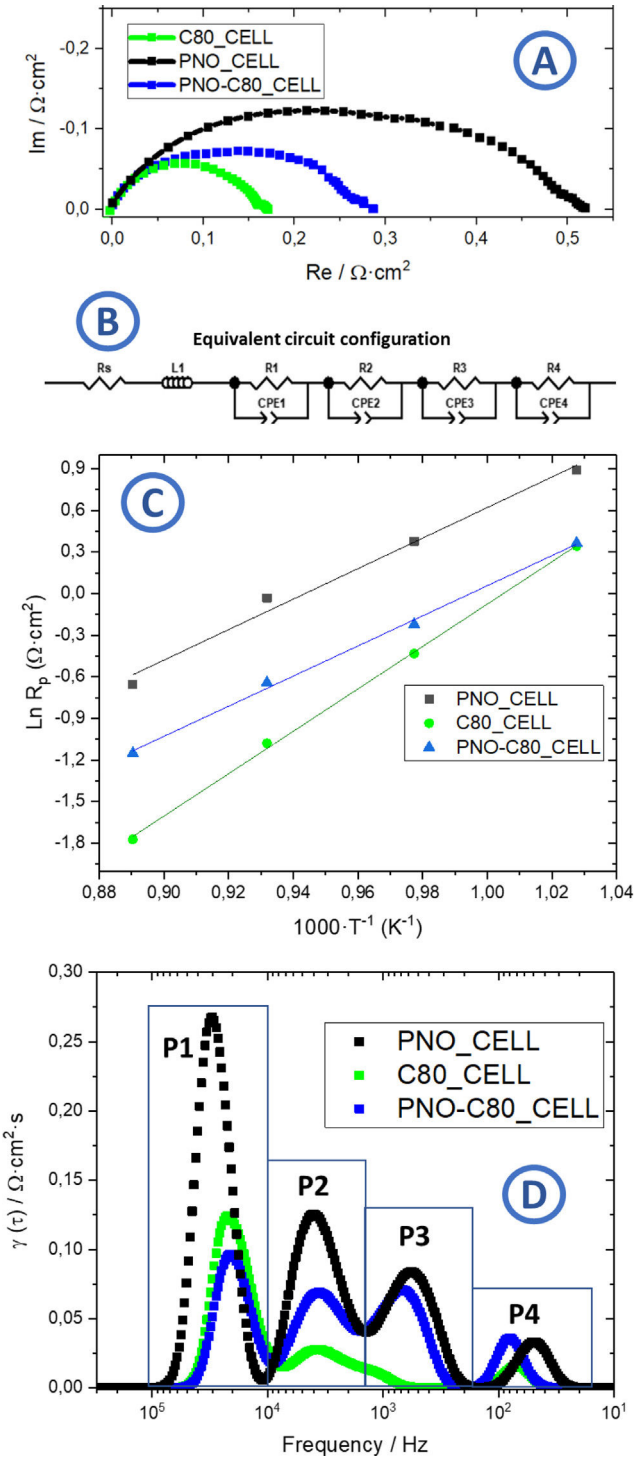

Fig. 5 – (a) Nyquist plot of C80 compared to PNO and double-layered electrodes at 850 °C. (b) Equivalent circuit configuration used in the DRT model. (c) Temperature dependences of R_{pol} in the temperature range of 700–850 °C of PNO and C80. (d) Distribution function of Relaxation Times at 850 °C of C80, PNO, and C80/PNO.

cells, peaks lower than 1 Hz did not appear likely due to the extension of the triple phase boundary area for electrochemical oxygen reduction reaction [74], which reduces the gas diffusion polarization resistance.

Comparing the cells below 800 °C (Fig. S.10 in the ESI), the processes that affect the R_{pol} in the frequency range of 10^3 Hz in C80 cell were rate-determining in peak P3, while for the PNO-C80 cell the most limiting process was P4. It was observed that the PNO layer has a detrimental effect on the oxygen surface exchange product of a lack of oxygen dissociation in the air electrode [75]. It is concluded that the polarization resistance values calculated at below 10^3 Hz dominated the total resistances of the cell and hindered the ionic diffusion of the electrochemical reaction. Below 10^2 Hz and 800 °C, oxygen diffusion becomes the dominant peak in terms of contribution to the R_{pol}. The activation energy of the R_{pol} calculated for PNO-C80 cell (106.0 ± 3.8 kJ mol^{-1}) is in line with the calculated for PNO cell (103.9 ± 8.3 kJ mol^{-1}), which is an indication of a major influence of the PNO layer in the active electrochemical zone of the double-layered electrodes. The activation energy of R_{pol} in the PNO_CELL cell, although higher than our calculations for k_{ex} and D_{chem}, is compatible with other authors' reported values in Table 2.

On the other hand, as observed in Section 3.2, the C80 sample significantly improved its oxygen surface exchange at 800 °C. This was observed in the reduction of peak P3 at this temperature, which is almost eliminated in the C80 cell at 850 °C. Similarly, the oxygen diffusion, as evidenced by P4 peaks at each temperature, is diminished for the C80 cell. The rate-limiting mechanism of this electrode appears in peak P2, where O^{2-} surface exchange and ionic transfer at the electrolyte interface dominate.

In general, even though a significant reduction of the R_{pol} is obtained using PNO–GDC electrodes, further analyses in single SOCs are required under standard SOFC/SOEC operation to validate those findings.

Conclusions

PNO–GDC air electrodes were structurally and electrochemically characterized for their prospect as air electrodes for SOC applications. XRD analysis confirmed a single-phase CPGO formed in C80, whereas coexisting CPGO and PrO_x phases were identified in C20. Moreover, the surface exchange and chemical diffusion coefficients showed some of the highest values among doped ceria. The surface exchange measured by the k_{ex} values was 2.23×10^{-6} cm s^{-1} at 800 °C for C80. Similarly, the chemical diffusion coefficient D_{chem} in C80 was 7.61×10^{-8} cm^2 s^{-1} at the same temperature. The results indicate that PNO–GDC thermal expansion coefficients of 14.1×10^{-6} K^{-1} are more suitable in the 500–700 °C range with standard electrolyte materials, such as YSZ and GDC, and PNO oxygen electrodes. In any case, CPGO-based air electrodes showed an enhanced electrochemical performance over the C80/PNO double-layer air electrode, where we found R_{pol} values as low as 0.17 Ω cm^2 at 850 °C using a composition of C80 for the oxygen electrode, about three times less than in pure PNO electrodes. Given these findings, PNO–GDC mixtures are confirmed as excellent candidates as oxygen electrodes for SOFC/SOEC applications.

Authors' contributions

M.A. Morales-Zapata: writing-original draft, validation, formal analysis, visualization, conceptualization, and investigation; A. Larrea: writing-review & editing, supervision, resources, funding acquisition and conceptualization; M.A. Laguna-Bercero: writing-review & editing, supervision, resources, data curation, funding acquisition and conceptualization.

Conflicts of interest

There are no conflicts to declare.

Acknowledgments

This research has received funding from grants PID2022-137626OB-C31, funded by MCIN/AEI/10.13039/501100011033 FEDER, UE and grant DGA T02-23R, funded by Gobierno de Aragón. Furthermore, the use of Servicio General de Apoyo a la Investigación (SAI, University of Zaragoza) and the Advanced Microscopy Laboratory (LMA) are also acknowledged. This research was also supported by MCIN with funding from NextGenerationEU (PRTR-C17.I1) within the Planes Complementarios con CCAA (Area of Green Hydrogen and Energy) and it has been carried out in the CSIC Interdisciplinary Thematic Platform (PTI+) Transición Energética Sostenible + (PTI–TRANSENER+).

Appendix A. Supplementary data

Supplementary data associated with this article can be found, in the online version, at doi:10.1016/j.bsecv.2025.03.003.

REFERENCES

[1] J. Fergus, J. Hui, R. Li, X. Wilkinson, D.P. Zhang, Solid Oxide Fuel Cells: Materials Properties and Performance, 1st ed., CRC Press, 2009, http://dx.doi.org/10.1201/9781420088847.
[2] G. Kim, S. Wang, A.J. Jacobson, L. Reimus, P. Brodersen, C.A. Mims, Rapid oxygen ion diffusion and surface exchange kinetics in $PrBaCo_2O_{5+x}$ with a perovskite related structure and ordered a cations, J. Mater. Chem. 17 (2007) 2500–2505, http://dx.doi.org/10.1039/b618345j.
[3] E. Tropin, M. Ananyev, N. Porotnikova, A. Khodimchuk, S. Saher, A. Farlenkov, E. Kurumchin, D. Shepel, E. Antipov, S. Istomin, H. Bouwmeester, Oxygen surface exchange and diffusion in $Pr_{1.75}Sr_{0.25}Ni_{0.75}Co_{0.25}O_{4\pm\delta}$, Phys. Chem. Chem. Phys. 21 (2019) 4779–4790, http://dx.doi.org/10.1039/c9cp00172g.
[4] V.A. Sadykov, V.S. Muzykantov, N.F. Yeremeev, V.V. Pelipenko, E.M. Sadovskaya, A.S. Bobin, Y.E. Fedorova, D.G. Amanbaeva, A.L. Smirnova, Solid Oxide fuel cell cathodes: importance of chemical composition and morphology, Catal. Sustain. Energy 2 (2016) 57–70, http://dx.doi.org/10.1515/cse-2015-0004.

[5] E. Boehm, J.M. Bassat, P. Dordor, F. Mauvy, J.C. Grenier, P. Stevens, Oxygen diffusion and transport properties in non-stoichiometric $Ln_{2-x}NiO_{4+\delta}$ oxides, Solid State Ion. 176 (2005) 2717–2725, http://dx.doi.org/10.1016/j.ssi.2005.06.033.

[6] A. Montenegro-Hernández, J. Vega-Castillo, L. Mogni, A. Caneiro, Thermal stability of $Ln_2NiO_{4+\delta}$ (Ln: La, Pr, Nd) and their chemical compatibility with YSZ and CGO solid electrolytes, Int. J. Hydrogen Energy 36 (2011) 15704–15714, http://dx.doi.org/10.1016/j.ijhydene.2011.08.105.

[7] A. Egger, N. Schrödl, C. Gspan, W. Sitte, $La_2NiO_{4+\delta}$ as electrode material for solid oxide fuel cells and electrolyzer cells, Solid State Ion. 299 (2017) 18–25, http://dx.doi.org/10.1016/j.ssi.2016.10.002.

[8] M.A. Morales-Zapata, M.A. Laguna-Bercero, A. Larrea, Lanthanide nickelates for their application on Solid Oxide Cells, Electrochim. Acta 444 (2023) 141970, http://dx.doi.org/10.1016/j.electacta.2023.141970.

[9] C. Ferchaud, J.C. Grenier, Y. Zhang-Steenwinkel, M.M.A. Van Tuel, F.P.F. Van Berkel, J.M. Bassat, High performance praseodymium nickelate oxide cathode for low temperature solid oxide fuel cell, J. Power Sources 196 (2011) 1872–1879, http://dx.doi.org/10.1016/j.jpowsour.2010.09.036.

[10] R. Chiba, H. Ishii, $Pr_2NiO_{4+\delta}$ cathode properties and reaction at interface with ceria and zirconia, ECS Trans. 68 (2015) 947–955, http://dx.doi.org/10.1149/06801.0947ecst.

[11] C.Y. Tsai, C.M. McGilvery, A. Aguadero, S.J. Skinner, Phase evolution and reactivity of $Pr_2NiO_{4+\delta}$ and $Ce_{0.9}Gd_{0.1}O_{2-\delta}$ composites under solid oxide cell sintering and operation temperatures, Int. J. Hydrogen Energy 44 (2019) 31458–31465, http://dx.doi.org/10.1016/j.ijhydene.2019.10.011.

[12] M.A. Laguna-Bercero, H. Monzón, A. Larrea, V.M. Orera, Improved stability of reversible solid oxide cells with a nickelate-based oxygen electrode, J. Mater. Chem. A Mater. 4 (2016), http://dx.doi.org/10.1039/c5ta08531d.

[13] M.A. Morales-Zapata, A. Larrea, M.A. Laguna-Bercero, Reversible operation performance of microtubular solid oxide cells with a nickelate-based oxygen electrode, Int. J. Hydrogen Energy 45 (2020) 5535–5542, http://dx.doi.org/10.1016/j.ijhydene.2019.05.122.

[14] R. Chockalingam, A.K. Ganguli, S. Basu, Praseodymium and gadolinium doped ceria as a cathode material for low temperature solid oxide fuel cells, J. Power Sources 250 (2014) 80–89, http://dx.doi.org/10.1016/j.jpowsour.2013.10.105.

[15] E. Dogdibegovic, J. Templeton, J. Yan, J.W. Stevenson, X.-D. Zhou, Compatibility of praseodymium nickelates with various cathode current collectors and electrolytes, ECS Trans. 57 (2013) 1761–1770, http://dx.doi.org/10.1149/05701.1761cst.

[16] J. Zhang, C. Lenser, N.H. Menzler, O. Guillon, Comparison of solid oxide fuel cell (SOFC) electrolyte materials for operation at 500 °C, Solid State Ion. 344 (2020) 115138, http://dx.doi.org/10.1016/j.ssi.2019.115138.

[17] E. Dogdibegovic, N.S. Alabri, C.J. Wright, J.S. Hardy, C.A. Coyle, S.A. Horlick, W. Guan, J.W. Stevenson, X.-D. Zhou, Activity and stability of $(Pr_{1-x}Nd_x)_2NiO_4$ as cathodes for solid oxide fuel cells: Part V. In situ studies of phase evolution, J. Electrochem. Soc. 164 (2017) F1115–F1121, http://dx.doi.org/10.1149/2.1707104es.

[18] T. Miki, T. Ogawa, M. Haneda, N. Kakuta, A. Ueno, S. Tateishi, S. Matsuura, M. Sato, Enhanced oxygen storage capacity of cerium oxides in $CeO_2/La_2O_3/Al_2O_3$ containing precious metals, J. Phys. Chem. 94 (1990) 6464–6467, http://dx.doi.org/10.1021/j100379a056.

[19] A.D. Logan, M. Shelef, Oxygen availability in mixed cerium/praseodymium oxides and the effect of noble metals, J. Mater. Res. 9 (1994) 468–475, http://dx.doi.org/10.1557/JMR. 1994.0468.

[20] T. Takasu, T. Sugino, Y. Matsuda, Electrical conductivity of praseodymia doped ceria, J. Appl. Electrochem. 14 (1984) 79–81, http://dx.doi.org/10.1007/BF00611261.

[21] C. Ftikos, M. Nauer, B.C.H. Steele, Electrical conductivity and thermal expansion of ceria doped with Pr, Nb and Sn, J. Eur. Ceram. Soc. 12 (1993) 267–270, http://dx.doi.org/10.1016/0955-2219(93)90101-V.

[22] R. Chiba, H. Taguchi, T. Komatsu, H. Orui, K. Nozawa, H. Arai, High temperature properties of $Ce_{1-x}Pr_xO_{2-\delta}$ as an active layer material for SOFC cathodes, Solid State Ion. 197 (2011) 42–48, http://dx.doi.org/10.1016/j.ssi.2011.03.022.

[23] S. Cheng, C. Chatzichristodoulou, M. Søgaard, A. Kaiser, P.V. Hendriksen, Ionic/electronic conductivity, thermal/chemical expansion and oxygen permeation in Pr and Gd Co-doped ceria $Pr_xGd_{0.1}Ce_{0.9-x}O_{1.95-\delta}$, J. Electrochem. Soc. 164 (2017) F1354–F1367, http://dx.doi.org/10.1149/2.0531713jes.

[24] D.P. Fagg, I.P. Marozau, A.L. Shaula, V.V. Kharton, J.R. Frade, Oxygen permeability, thermal expansion and mixed conductivity of $Gd_xCe_{0.8-x}Pr_{0.2}O_{2-\delta}$, $x = 0$, 0.15, 0.2, J. Solid State Chem. 179 (2006) 3347–3356, http://dx.doi.org/10.1016/j.jssc.2006.06.028.

[25] B.A. Boukamp, M.W. Den Otter, H.J.M. Bouwmeester, Transport processes in mixed conducting oxides: combining time domain experiments and frequency domain analysis, J. Solid State Electrochem. 8 (2004) 592–598, http://dx.doi.org/10.1007/s10008-003-0493-6.

[26] J. Rodríguez-Carvajal, Recent advances in magnetic structure determination by neutron powder diffraction, Phys. B: Phys. Condens. Matter 192 (1993) 55–69, http://dx.doi.org/10.1016/0921-4526(93)90108-I.

[27] FIZ Karlsruhe, ICSD Database, About ICSD (n.d.). https://icsd.products.fiz-karlsruhe.de/en/about/about-icsd [accessed 15.11.24].

[28] G. Cliff, G.W. Lorimer, The quantitative analysis of thin specimens, J. Microsc. 103 (1975) 203–207, https://onlinelibrary.wiley.com/doi/abs/10.1111/j.1365-2818.1975.tb03895.x.

[29] R.F. Egerton, Electron Energy-Loss Spectroscopy in the Electron Microscope, 3rd ed., Springer, New York, 2011.

[30] F. Ciucci, Electrical conductivity relaxation measurements: statistical investigations using sensitivity analysis, optimal experimental design and ECRTOOLS, Solid State Ion. 239 (2013) 28–40, http://dx.doi.org/10.1016/j.ssi.2013.03.020.

[31] J. Andreas Schuler, H. Lübbe, A. Hessler-Wyser, J. Van Herle, Nd-nickelate solid oxide fuel cell cathode sensitivity to Cr and Si contamination, J. Power Sources 213 (2012) 223–228, http://dx.doi.org/10.1016/j.jpowsour.2012.03.112.

[32] D. Mccullough, An X-ray study of rare-earth oxide systems, J. Am. Chem. Soc. 72 (1949) 1386–1390.

[33] L. Barrio, A. Kubacka, G. Zhou, M. Estrella, A. Martínez-Arias, J.C. Hanson, M. Fernández-García, J.A. Rodriguez, Unusual physical and chemical properties of Ni in $Ce_{1-x}Ni_xO_{2-y}$ oxides: structural characterization and catalytic activity for the water gas shift reaction, J. Phys. Chem. C 114 (2010) 12689–12697, http://dx.doi.org/10.1021/jp103958u.

[34] J. Kojčinović, D. Tatar, S. Šarić, C. Bartus Pravda, A. Mavrič, I. Arčon, Z. Jagličić, M. Mellin, M. Einert, A. Altomare, R. Caliandro, Á. Kukovecz, J.P. Hofmann, I. Djerdj, Resolving a structural issue in cerium-nickel-based oxide: a single compound or a two-phase system? Dalton Trans. 53 (2023) 2082–2097, http://dx.doi.org/10.1039/d3dt03280a.

[35] J.A. Fortner, E.C. Buck, A.J.G. Ellison, J.K. Bates, EELS analysis of redox in glasses for plutonium immobilization, Ultramicroscopy 67 (1997) 77–81, http://dx.doi.org/10.1016/S0304-3991(96)00108-8.

[36] L. Wu, H.J. Wiesmann, A.R. Moodenbaugh, R.F. Klie, Y. Zhu, D.O. Welch, M. Suenaga, Oxidation state and lattice

expansion of CeO_{2-x} nanoparticles as a function of particle size, Phys. Rev. B Condens. Matter Mater. Phys. 69 (2004) 1–9, http://dx.doi.org/10.1103/PhysRevB.69.125415.
[37] A. Orera, F. Wang, E. Ferreiro-Vila, S. Serrano-Zabaleta, A. Larrañaga, M.A. Laguna-Bercero, E.C. Dickey, F. Rivadulla, M.C. Muñoz, Á. Larrea, Interfacial stability and ionic conductivity enhanced by dopant segregation in eutectic ceramics: the role of Gd segregation in doped CeO_2/CoO and CeO_2/NiO interfaces, J. Mater. Chem. A Mater. 8 (2020) 2591–2601, http://dx.doi.org/10.1039/c9ta12315f.
[38] B. Feng, I. Sugiyama, H. Hojo, H. Ohta, N. Shibata, Y. Ikuhara, Atomic structures and oxygen dynamics of CeO_2 grain boundaries, Sci. Rep. 6 (2016) 1–7, http://dx.doi.org/10.1038/srep20288.
[39] G. Niu, M.A. Schubert, F. D'Acapito, M.H. Zoellner, T. Schroeder, F. Boscherini, On the local electronic and atomic structure of $Ce_{1-x}Pr_xO_{2-\delta}$ epitaxial films on Si, J. Appl. Phys. 116 (2014) 0–9, http://dx.doi.org/10.1063/1.4896590.
[40] M. Schaube, R. Merkle, J. Maier, Oxygen exchange kinetics on systematically doped ceria: a pulsed isotope exchange study, J. Mater. Chem. A Mater. 7 (2019) 21854–21866, http://dx.doi.org/10.1039/c9ta05908c.
[41] W.C. Chueh, A.H. McDaniel, M.E. Grass, Y. Hao, N. Jabeen, Z. Liu, S.M. Haile, K.F. McCarty, H. Bluhm, F. El Gabaly, Highly enhanced concentration and stability of reactive Ce^{3+} on doped CeO_2 surface revealed in operando, Chem. Mater. 24 (2012) 1876–1882, http://dx.doi.org/10.1021/cm300574v.
[42] Q. Lu, G. Vardar, M. Jansen, S.R. Bishop, I. Waluyo, H.L. Tuller, B. Yildiz, Surface defect chemistry and electronic structure of $Pr_{0.1}Ce_{0.9}O_{2-\delta}$ revealed in operando, Chem. Mater. 30 (2018) 2600–2606, http://dx.doi.org/10.1021/acs.chemmater.7b05129.
[43] J.A. Fortner, E.C. Buck, The chemistry of the light rare-earth elements as determined by electron energy loss spectroscopy, Appl. Phys. Lett. 68 (1996) 3817–3819, http://dx.doi.org/10.1063/1.116627.
[44] P. Manoubi, T. Colliex, C. Rez, Quantitative electron energy loss spectroscopy on M45 edges in rare earth oxides, J. Electron. Spectrosc. Relat. Phenom. 50 (1990) 1–18, http://dx.doi.org/10.1016/0368-2048(90)80001-Q.
[45] D.J. Kim, Lattice Parameters, ionic conductivities, and solubility limits in fluorite-structure MO_2 oxide [M = Hf4+, Zr4+, Ce4+, Th4+ U4+] solid solutions, J. Am. Ceram. Soc. 72 (1989) 1415–1421, http://dx.doi.org/10.1111/j.1151-2916.1989.tb07663.x.
[46] A.V. Kuzmin, V.P. Gorelov, B.T. Melekh, M. Glerup, F.W. Poulsen, Phase transitions in undoped $BaCeO_3$, Solid State Ion. 162–163 (2003) 13–22, http://dx.doi.org/10.1016/S0167-2738(03)00247-9.
[47] A. Flura, S. Dru, C. Nicollet, V. Vibhu, S. Fourcade, E. Lebraud, A. Rougier, J.M. Bassat, J.C. Grenier, Chemical and structural changes in $Ln_2NiO_{4+\delta}$ (Ln = La, Pr or Nd) lanthanide nickelates as a function of oxygen partial pressure at high temperature, J. Solid State Chem. 228 (2015) 189–198, http://dx.doi.org/10.1016/j.jssc.2015.04.029.
[48] V. Vibhu, I.C. Vinke, R.A. Eichel, J.-M. Bassat, L.G.J. de Haart, Cobalt substituted lanthanide nickelates ($Ln_2Ni_{1-x}Co_xO_{4+\delta}$, Ln = La, Pr; x = 0, 0.1, 0.2) as high performance oxygen electrodes for solid oxide cells, ECS Trans. 91 (2019) 1327–1339.
[49] Z. Wu, Y. Cheng, F. Tao, L. Daemen, G.S. Foo, L. Nguyen, X. Zhang, A. Beste, A.J. Ramirez-Cuesta, Direct neutron spectroscopy observation of cerium hydride species on a cerium oxide catalyst, J. Am. Chem. Soc. 139 (2017) 9721–9727, http://dx.doi.org/10.1021/jacs.7b05492.
[50] C. Chatzichristodoulou, P.V. Hendriksen, A. Hagen, Defect chemistry and thermomechanical properties of $Ce_{0.8}Pr_xTb_{0.2-x}O_{2-\delta}$, J. Electrochem. Soc. 157 (2010) B299, http://dx.doi.org/10.1149/1.3270475.
[51] C. Berger, E. Bucher, A. Egger, A.T. Strasser, N. Schrödl, C. Gspan, J. Hofer, W. Sitte, Synthesis and characterization of the novel K_2NiF_4-type oxide $Pr_2Ni_{0.9}Co_{0.1}O_{4+\delta}$, Solid State Ion. 316 (2018) 93–101, http://dx.doi.org/10.1016/j.ssi.2017.12.024.
[52] D. Ning, A. Baki, T. Scherb, J. Song, A. Fantin, X. Liu, G. Schumacher, J. Banhart, H.J.M. Bouwmeester, Influence of A-site deficiency on structural evolution of $Pr_{2-x}NiO_{4+\delta}$ with temperature, Solid State Ion. 342 (2019), http://dx.doi.org/10.1016/j.ssi.2019.115056.
[53] S.J. Skinner, J.A. Kilner, Oxygen diffusion and surface exchange in $La_{2-x}Sr_xNiO_{4+\delta}$, Solid State Ion. 135 (2000) 709–712, http://dx.doi.org/10.1016/S0167-2738(00)00388-X.
[54] J.M. Bassat, P. Odier, A. Villesuzanne, C. Marin, M. Pouchard, Anisotropic ionic transport properties in $La_2NiO_{4+\delta}$ single crystals, Solid State Ion. 167 (2004) 341–347, http://dx.doi.org/10.1016/j.ssi.2003.12.012.
[55] H. Zhao, F. Mauvy, C. Lalanne, J.M. Bassat, S. Fourcade, J.C. Grenier, New cathode materials for ITSOFC: phase stability, oxygen exchange and cathode properties of $La_{2-x}NiO_{4+\delta}$, Solid State Ion. 179 (2008) 2000–2005, http://dx.doi.org/10.1016/j.ssi.2008.06.019.
[56] H.J.M. Bouwmeester, C. Song, J. Zhu, J. Yi, M. Van Sint Annaland, B.A. Boukamp, A novel pulse isotopic exchange technique for rapid determination of the oxygen surface exchange rate of oxide ion conductors, Phys. Chem. Chem. Phys. 11 (2009) 9640–9643, http://dx.doi.org/10.1039/b912712g.
[57] N.M. Porotnikova, A.V. Khodimchuk, M.V. Ananyev, V.A. Eremin, E.S. Tropin, A.S. Farlenkov, E.Y. Pikalova, A.V. Fetisov, Oxygen isotope exchange in praseodymium nickelate, J. Solid State Electrochem. 22 (2018) 2115–2126, http://dx.doi.org/10.1007/s10008-018-3919-x.
[58] V.A. Sadykov, N.F. Eremeev, E.M. Sadovskaya, A.S. Bobin, Y.E. Fedorova, V.S. Muzykantov, N.V. Mezentseva, G.M. Alikina, T.A. Kriger, V.D. Belyaev, V.A. Rogov, A.S. Ulikhin, Y.S. Okhlupin, N.F. Uvarov, O.F. Bobrenok, N. McDonald, J. Watton, A. Dhir, R. Steinberger-Wilckens, J. Mertens, I.C. Vinke, Cathodic materials for intermediate-temperature solid oxide fuel cells based on praseodymium nickelates–cobaltites, Russ. J. Electrochem. 50 (2014) 669–679, http://dx.doi.org/10.1134/S1023193514070131.
[59] S. Saher, J. Song, V. Vibhu, C. Nicollet, A. Flura, J.M. Bassat, H.J.M. Bouwmeester, Influence of annealing at intermediate temperature on oxygen transport kinetics of $Pr_2NiO_{4+\delta}$, J. Mater. Chem. A Mater. 6 (2018) 8331–8339, http://dx.doi.org/10.1039/c7ta08885j.
[60] M. Burriel, G. Garcia, J. Santiso, J.A. Kilner, R.J. Chater, S.J. Skinner, Anisotropic oxygen diffusion properties in epitaxial thin films of $La_2NiO_{4+\delta}$, J. Mater. Chem. 18 (2008) 416–422, http://dx.doi.org/10.1039/b711341b.
[61] C. Nicollet, C. Toparli, G.F. Harrington, T. Defferriere, B. Yildiz, H.L. Tuller, Acidity of surface-infiltrated binary oxides as a sensitive descriptor of oxygen exchange kinetics in mixed conducting oxides, Nat. Catal. 3 (2020) 913–920, http://dx.doi.org/10.1038/s41929-020-00520-x.
[62] A. Egger, E. Bucher, M. Yang, W. Sitte, Comparison of oxygen exchange kinetics of the IT-SOFC cathode materials $La_{0.5}Sr_{0.5}CoO_{3-\delta}$ and $La_{0.6}Sr_{0.4}CoO_{3-\delta}$, Solid State Ion. 225 (2012) 55–60, http://dx.doi.org/10.1016/j.ssi.2012.02.050.
[63] P.S. Manning, J.D. Sirman, J.A. Kilner, Oxygen self-diffusion and surface exchange studies of oxide electrolytes having the fluorite structure, Solid State Ion. 93 (1996) 125–132, http://dx.doi.org/10.1016/s0167-2738(96)00514-0.
[64] E. Ruiz-Trejo, J.D. Sirman, Y.M. Baikov, J.A. Kilner, Oxygen ion diffusivity, surface exchange and ionic conductivity in single crystal Gadolinia doped Ceria, Solid State Ion. 113–115 (1998) 565–569, http://dx.doi.org/10.1016/s0167-2738(98)00323-3.
[65] J.A. Kilner, C.K.M. Shaw, Mass transport in $La_2Ni_{1-x}Co_xO_{4+\delta}$ oxides with the K_2NiF_4 structure, Solid State Ion. 154–155

(2002) 523–527, http://dx.doi.org/10.1016/S0167-2738(02)00506-4.
[66] H.L. Tuller, S.R. Bishop, D. Chen, Y. Kuru, J.J. Kim, T.S. Stefanik, Praseodymium doped ceria: model mixed ionic electronic conductor with coupled electrical, optical, mechanical and chemical properties, Solid State Ion. 225 (2012) 194–197, http://dx.doi.org/10.1016/j.ssi.2012.02.029.
[67] S. Lübke, H.D. Wiemhöfer, Electronic conductivity of Gd-doped ceria with additional Pr-doping, Solid State Ion. 117 (1999) 229–243, http://dx.doi.org/10.1016/s0167-2738(98)00408-1.
[68] D.P. Fagg, V.V. Kharton, J.R. Frade, Transport in ceria electrolytes modified with sintering aids: effects on oxygen reduction kinetics, J. Solid State Electrochem. 8 (2004) 618–625, http://dx.doi.org/10.1007/s10008-004-0509-x.
[69] D. Chen, S.R. Bishop, H.L. Tuller, Praseodymium-cerium oxide thin film cathodes: study of oxygen reduction reaction kinetics, J. Electroceram. 28 (2012) 62–69, http://dx.doi.org/10.1007/s10832-011-9678-z.
[70] K. Schmale, M. Grünebaum, M. Janssen, S. Baumann, F. Schulze-Küppers, H.D. Wiemhöfer, Electronic conductivity of $Ce_{0.8}Gd_{0.2-x}Pr_xO_{2-\delta}$ and influence of added CoO, Phys. Status Solidi B Basic Res. 248 (2011) 314–322, http://dx.doi.org/10.1002/pssb.201046365.
[71] T.S. Stefanik, H.L. Tuller, Nonstoichiometry and defect chemistry in praseodymium-cerium oxide, J. Electroceram. 13 (2004) 799–803, http://dx.doi.org/10.1007/s10832-004-5195-7.
[72] M. Ghamarinia, A. Babaei, C. Zamani, H. Aslannejad, Application of the distribution of relaxation time method in electrochemical analysis of the air electrodes in the SOFC/SOEC devices: a review, Chem. Eng. J. Adv. 15 (2023), http://dx.doi.org/10.1016/j.ceja.2023.100503.
[73] J.G. Railsback, Z. Gao, S.A. Barnett, Oxygen electrode characteristics of $Pr_2NiO_{4+\delta}$-infiltrated porous $(La_{0.9}Sr_{0.1})(Ga_{0.8}Mg_{0.2})O_{3-\delta}$, Solid State Ion. 274 (2015) 134–139, http://dx.doi.org/10.1016/j.ssi.2015.03.030.
[74] M. Shah, S.A. Barnett, Solid oxide fuel cell cathodes by infiltration of $La_{0.6}Sr_{0.4}Co_{0.2}Fe_{0.8}O_{3-\delta}$ into Gd-Doped Ceria, Solid State Ion. 179 (2008) 2059–2064, http://dx.doi.org/10.1016/j.ssi.2008.07.002.
[75] A.R. Gilev, E.A. Kiselev, M.E. Ozhiganov, V.A. Cherepanov, Polarization resistance of the Ruddlesden–Popper nickelates $La_{n+1}Ni_nO_{3n+1}$ ($n = 1\ 2, 3$): comparative analysis using the distribution of relaxation times method, Solid State Ion. 386 (2022), http://dx.doi.org/10.1016/j.ssi.2022.116032.